Quantifying the dynamic spreading of a molten sand droplet using multiphase mesoscopic simulations

Rahul Babu Koneru * and Alison Flatau

Department of Aerospace Engineering, University of Maryland, College Park, Maryland 20742, USA

Zhen Li 10 †

Department of Mechanical Engineering, Clemson University, Clemson, South Carolina 29634, USA

Luis Bravo, Muthuvel Murugan, and Anindya Ghoshal
Weapons and Materials Research Directorate, DEVCOM Army Research Laboratory, Aberdeen Proving
Ground, Maryland 21005, USA

George Em Karniadakis

Division of Applied Mathematics, Brown University, Providence, Rhode Island 02912, USA

(Received 25 May 2022; accepted 12 September 2022; published 4 October 2022)

Upon coming into contact with a solid surface, a liquid droplet spreads rapidly during the early moments due to inertial/capillary effects before the viscous dissipation slows it down. The temporal evolution of the spreading radius depends on the viscosity of the liquid drop. For low-viscosity liquids, the spreading radius follows a power-law, whereas for higher viscosity liquids it scales linearly with time with additional logarithmic corrections. In this work, the spreading dynamics of molten sand is investigated at isothermal conditions. The molten sand is a mixture of Calcia, Magnesia, Alumina, and Silicate, commonly referred to as CMAS, and is characterized by large viscosity, density, and surface tension. The multiphase many-body dissipative particle dynamics (mDPD) model is carefully parameterized to simulate a highly viscous molten CMAS droplet at 1260 °C. Three-dimensional (3D) simulations were carried out at different initial drop sizes and equilibrium contact angles. Despite its unique properties, the spreading behavior of molten CMAS is in good agreement with theory and experiments of viscous coalescence of drops. Importantly, the two distinct spreading regimes are observed in the mDPD simulations. Due to the large viscosity, a slower but a nonunique spreading rate is observed in the inertial regime. However, the spreading rate in the viscous regime is in agreement with Tanner's law. The spreading radius remains unaffected by the initial drop size and collapses onto a master curve under viscous time scaling in agreement with theory and experiments. For different equilibrium angles, the spreading rate is observed to be nearly identical in the inertial regime. This indicates a universal spreading behavior during the early stages of spreading unaffected by both the initial drop size and the equilibrium contact angle. The contact line velocity was also computed to assess its relation with the dynamic contact angle. The dynamic contact angle data collapse when plotted as a function of the capillary number, displaying a remarkable agreement with Hoffman's description of dynamic contact angle evolution.

DOI: 10.1103/PhysRevFluids.7.103602

^{*}rkoneru@umd.edu

[†]zli7@clemson.edu

I. INTRODUCTION

Droplets will start spreading on a solid surface as the liquid contacts with a surface. Droplet spreading and wettability play a crucial role in many engineering processes and have garnered renewed attention due to their importance in self-cleaning [1], fabrication of microelectromechanical systems [2] (MEMS), microfluidic devices [3], and high-quality inkjet printing [4]. The spreading process is dictated by the capillary and the viscous forces and is a simple exercise in minimization of potential and surface energies of the drop. The dynamic spreading of simple liquids, i.e., water, water/glycerin mixtures, silicone oils, etc., has been extensively studied using experiments [5–8] and numerical simulations [9–11]. Bianche et al. [5] observed that the spreading of a completely wetting drop on a solid surface is analogous to droplet coalescence which has been studied in great detail. Analytical solutions, based on Stokesian dynamics, have also been derived for the growth of the radius at the neck between two coalescing droplets. Generally, the radius of the spreading area follows a power law of the form $r \sim t^{\alpha}$ and is composed of two distinct regimes, an inertial regime and a viscous regime. In the inertial regime, the large gradient of the interface curvature drives the contact line and is resisted by the inertia of the drop. At this stage, the Laplace pressure drives a capillary wave across the droplet surface. Once the capillary waves dissipate, the spreading enters the viscous regime where the driving force is balanced by the viscous friction. When the effects of gravity are negligible, a pure water drop spreads at a rate of $t^{1/2}$ in the inertial regime and $t^{1/10}$ in the viscous regime. The spreading rate in the viscous regime corresponds to the well-known Tanner's law. However, the spreading rate of more viscous drops was observed to vary between 0 and 1 in the inertial regime along with a logarithmic dependence on r as shown in Eq. (1), while Tanner's law was observed in the viscous regime [8]. This is the solution of the Stokes flow of two viscous drops coalescing when the viscosity of the surrounding fluid is negligible [12]:

$$\frac{r}{R} \sim \frac{t}{(\mu R/\sigma)} \ln\left(\frac{r}{R}\right). \tag{1}$$

In the case of partial wettability, another factor that determines the spreading rate is the equilibrium contact angle. In the case of low-viscosity liquids [7], drops with a smaller equilibrium contact angles were observed to spread faster compared to drops with larger equilibrium contact angles. It should be noted that in these experiments the spreading was inertial/capillary dominated. When the spreading is viscous dominated [6], the spreading in the inertial regime was observed to be independent of the equilibrium contact angle. This is consistent with the spreading-coalescence analog. Another important aspect of wettability is the evolution of the contact angle in relation to the speed of the contact line. This determines the shape of the interface which is important in determining the boundary conditions. In fact, there are analytical expressions [13] (based on asymptotic expansions) describing the evolution of the apparent contact angle (θ_{ap}) as a function of the capillary number which is defined as $Ca = \mu u_{cl}/\sigma$ where u_{cl} is the velocity of the contact line, μ is the dynamic viscosity and σ is the surface tension. These expressions generally take the form $\theta_D \sim Ca^{1/3}$ for Ca < 1, where θ_D is the dynamic contact angle. Additionally, approximate and empirical expressions, based on experiments, have also been developed [14,15].

Most of the previous studies of drop spreading on solid surfaces focused on relatively low viscous fluids [16], while much less is known about the dynamics of spreading and wetting of highly viscous fluids, i.e., greater than 1000 times the viscosity of water, such as a lot of molten materials in 3D printing [17]. One particular area where the high-viscous fluids play an important role and which is the subject of research in this paper pertains to the deposition of molten sand particulates in gas turbine engines (GTEs) [18]. Rotorcrafts operating in dusty environments suffer structural damage due to the ingestion of solid particulates into the gas turbine engines. The ingested particles can cause erosion due to repeated impact, accumulate in air pathways leading to blockages and cause material degradation due to the molten particulate deposits on the hotsection components of the GTE. Environmental barrier coatings (EBC) offer protection against kinetic impacts while the inertial particle separators filter out larger particles (>75 μ m) without

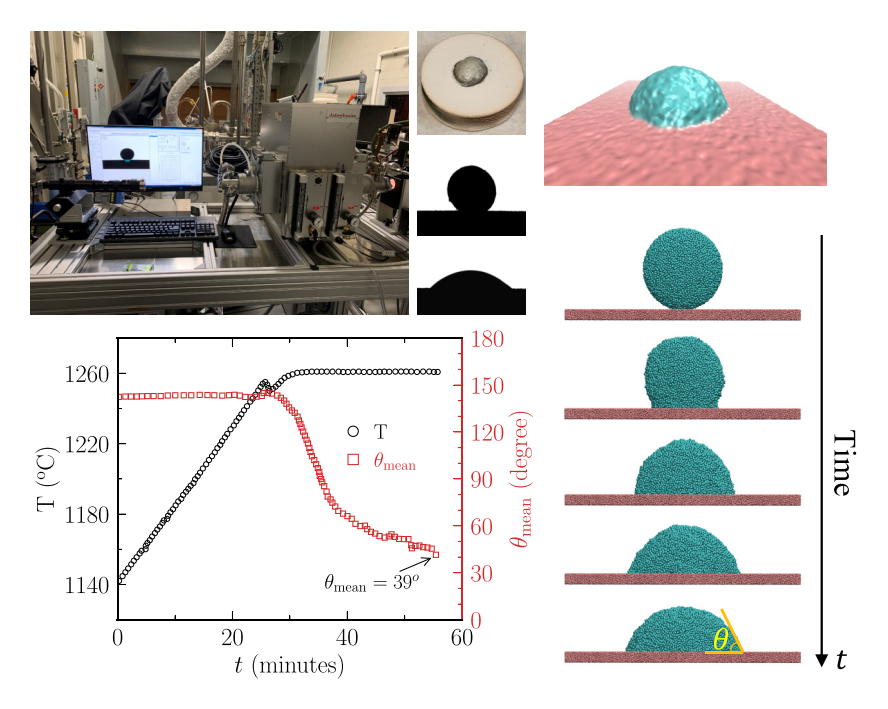


FIG. 1. Left: Experimental measurement of the evolution of temperature T and wetting contact angle θ_{mean} of a molten CMAS drop, where the molten temperature of the CMAS is 1260 °C. Right: the setup of multiphase DPD simulations of a 3D CMAS droplet spreading dynamics (isothermal process) on a hydrophilic surface with equilibrium contact angle $\theta_{\text{eq}} = 39^{\circ}$.

a significant pressure drop at the compressor inlet. Smaller particles, however, pass through the cold section and melt in the combustion chamber. The molten particulates, primarily composed of the oxides of calcia-magnesia-alumina-silica (CMAS), adhere to and damage the thermal barrier coating (TBC) on the hot-section components. The molten CMAS material has been observed to infiltrate, react chemically with the thermal barrier coating and solidify into a glassy coating as it cools down. This is referred to as "CMAS attack" [19]. In addition to the structural damage, the CMAS penetration has also been observed to alter the thermal properties of the TBCs such as volumetric heat capacity and thermal conductivity [20]. Some of the mitigation strategies involve tailoring the TBC microstructure [21,22], accelerating the chemical reaction time between the molten CMAS deposit and the coating to induce solidification and thus prevent penetration [19]. With the performance envelope of the GTEs ever expanding, the operating temperatures are bound to increase which will only exacerbate CMAS attack. From a hydrodynamic point of view, it is important to understand the fundamental process of droplet spreading to gain more insight into CMAS attack and aid in the development of tailored functionalized surfaces [23,24].

The viscosity of CMAS is a strong function of temperature which reduces nonlinearly with an increase in temperature [22]. A molten CMAS drop is more than 3000 times viscous (at 1260 °C) than a water drop and the surface tension is 6.4 times larger than the water-air surface tension. The large viscosity and surface tension of CMAS provide an interesting regime of fluid phenomena in itself but owing to its importance in understanding the CMAS attack on TBCs it is crucial to understand the spreading dynamics. Toward developing a more fundamental insight into the spreading dynamics of molten CMAS, a detailed numerical study is carried-out using the many-body dissipative particle dynamics (mDPD) framework, which is a multiphase extension of dissipative particle dynamics (DPD) [25]. As shown in Fig. 1, experiments were performed at

the high-temperature contact angle facility at the Army Research Laboratory (ARL) in Aberdeen Proving Ground to measure the equilibrium contact angle of a molten CMAS drop on a flat ceramic coating surface. With a linear increase of temperature to the melting point of CMAS and then holding it at 1260 °C for 40 min, the contact angle of a CMAS drop reaches to $\theta_{eq} = 39^{\circ} \pm 1^{\circ}$ at the end of the experiment. In the experiment, spreading and melting processes are coupled and the CMAS infiltrates into the coating. To simplify the problem and focus on the spreading dynamics of the highly viscous CMAS drop, we consider an isothermal process and simulate the spreading dynamics of a 3D CMAS drop using the mesoscale mDPD method, which is able to accurately capture the contact line motion under the thermodynamic fluctuations as demonstrated in many previous mDPD simulations of droplet dynamics [26-29]. Although the emphasis is not laid upon the role of thermodynamic fluctuations on the contact line dynamics in this work, the primary reason for choosing the mDPD framework, over other particle-based and continuum-based methods, lies in the fact that the constitutive relation need not be prescribed in this framework. The spreading and infiltration dynamics of molten CMAS have been investigated numerically by several groups. Recently, Munuhe et al. [30] investigated CMAS spreading and infiltration into porous TBC under nonisothermal conditions using the lubrication theory in a two-dimensional (2D) axisymmetric configuration. Kabir et al. [31] employed a volume-of-fluid method to study CMAS infiltration into "feathery" microstructures in a 2D geometry. The spreading of molten CMAS on smooth substrates following an impact at a high velocity (up to 250 m/s) was systematically investigated by Chaussonnet et al. [32] for different CMAS morphologies and physical properties using the smoothed particle hydrodynamics (SPH) method. In all these studies, the molten droplet was treated as a Newtonian fluid and in the absence of experimental data on the exact rheology of molten CMAS, the aforementioned advantage of mDPD allows for a better representation of the underlying fluid dynamics. In fact, Song et al. [33] reported that molten drops of volcanic ash remain heterogenous, possibly due to the presence of crystals and bubbles, below a temperature of 1315 °C thereby implying a non-Newtonian nature of the melts.

DPD is a mesoscopic simulation method developed to study hydrodynamic phenomena [34]. Lately, mDPD has been widely used to study multiphase phenomena in soft-matter and rheological problems [35]. In this method, each mDPD particle is a collection of atoms/molecules which are alike. The system is representative of a coarse-grained molecular dynamics (MD) method and can be rigorously derived from microscopic dynamics [36] as well as from fluctuating Navier-Stokes equation [37]. Compared to MD, mDPD by design offers the advantage of taking larger integration time-steps due to the soft interaction potentials [38]. The moving contact line (MCL) creates a nonintegrable stress singularity at the solid-liquid boundary and requires a special treatment in continuum-based models [39]. Typically, cutoffs are introduced at molecular and capillary length scales to deal with the singularity. Incidentally, this does not pose a problem to particle-based methods such as the one used in this work. At the solid-liquid interface, the no-slip boundary condition developed for arbitrary-shaped geometries [40] is used in this work. In this work, sessile drop simulations of molten CMAS at different radii and equilibrium contact angles are carried-out at isothermal conditions. A previous experiment performed by Eddi *et al.* [8] is also used to compare the spreading rates of the drop obtained in mDPD simulations.

The layout of this paper is as follows: The numerical method is introduced briefly in Sec. II and is followed by a discussion on the simulation setup and parameter mapping in Sec. III. The results describing the evolution of the contact area radius and the dynamic contact angle behavior are presented in Sec. IV. Finally, the findings are summarized in Sec. V.

II. GOVERNING EQUATIONS

The interactions between mDPD particles are considered pairwise and their motion is governed by the Newton's second law of motion [41]. The position and velocity of the *i*th mDPD particle is

tracked using

$$\frac{d\mathbf{r}_i}{dt} = \mathbf{v}_i, \ m_i \frac{d\mathbf{v}_i}{dt} = \mathbf{F}_i = \sum_{i \neq i} \mathbf{F}_{ij}^D + \mathbf{F}_{ij}^R + \mathbf{F}_{ij}^C,$$
(2)

where m_i denotes the mass of the particle i, \mathbf{r}_i , \mathbf{v}_i , and \mathbf{F}_i are its position, velocity, and force vectors, respectively. The total force \mathbf{F}_i is taken to be the linear superposition of the dissipative (\mathbf{F}_{ij}^D) , random (\mathbf{F}_{ii}^R) , and conservative forces (\mathbf{F}_{ij}^C) between neighboring particles i and j, which are computed by

$$\mathbf{F}_{ij}^{C} = A\omega_c(r_{ij})\mathbf{e}_{ij} + B(\rho_i + \rho_j)\omega_d(\mathbf{r}_{ij})\mathbf{e}_{ij}, \tag{3}$$

$$\mathbf{F}_{ij}^{D} = -\gamma \omega_D(r_{ij})(\mathbf{e}_{ij} \cdot \mathbf{v}_{ij})\mathbf{e}_{ij}, \tag{4}$$

$$\mathbf{F}_{ij}^{R} = \beta \omega_{R}(r_{ij})(dt)^{-1/2} \xi_{ij} \mathbf{e}_{ij}, \tag{5}$$

where $\omega_{(*)}$ is a weighting function which depends on the relative distance $r_{ij} = |\mathbf{r}_i - \mathbf{r}_j|$ between the two particles i and j. These forces have a compact support and vanish beyond a cutoff distance r_c . The constants γ , β , A, and B determine the strengths of each individual force. The relative velocity between a pair of particles is given by $\mathbf{v}_{ij} = \mathbf{v}_i - \mathbf{v}_j$. The forces between a pair of particles always lie along the line of centers $\mathbf{e}_{ij} = \mathbf{r}_{ij}/r_{ij}$. The Gaussian white noise ξ_{ij} is a random variable drawn from a Gaussian distribution with $\langle \xi_{ij}(t) \rangle = 0$ and $\langle \xi_{ij}(t) \xi_{kl}(t') \rangle = (\delta_{ik}\delta_{jl} + \delta_{il}\delta_{jk})\delta(t - t')$ where δ_{ij} is the Kronecker δ and $\delta(t - t')$ is the Dirac δ function [42].

By design, a mDPD system is isothermal and the thermal equilibrium of the system is dependent on the fluctuating and dissipative forces. In the presence of these forces, the system should recover the canonical Gibbs-Boltzmann distribution [42]. This is referred to as the fluctuating-dissipation theorem (FDT) [41] and leads to the following relation between the weights and the strengths of these two forces:

$$\omega_D = \omega_R^2, \ \beta^2 = 2\gamma k_B T, \tag{6}$$

where $\omega_D = \omega_R^2 = (1 - r_{ij}/r_D)^s$ with s = 0.5, $r_D = 1.45$, and the nondimensional temperature $k_BT = 1.0$, where k_B is the Boltzmann constant. At a molecular scale, the random (Brownian) motion of particles persists even at thermal equilibrium leading to tiny thermal fluctuations. The fluctuation-dissipation theorem ensures that these fluctuations remain bounded even under the action of an external force via a dissipative force. This is what is referred to as the thermal equilibrium. The nondimensional temperature, which remains a constant, affects the magnitude of the random force. Throughout the course of the simulation, Eq. (6) is satisfied for all the pairwise interactions. In many-body interactions, the conservative force is dependent on an attractive force and a local density (ρ) dependent repulsive force. The local density of a particle is computed as weighted sum of its neighbors, i.e., $\rho_i = \sum \omega_\rho(r_{ij})$. In this work, ω_ρ is the Lucy kernel and is defined as [43]

$$\omega_{\rho}(r_{ij}) = \frac{105}{16\pi r_{c\rho}^3} \left(1 + \frac{3r_{ij}}{r_{c\rho}} \right) \left(1 - \frac{r_{ij}}{r_{c\rho}} \right)^3. \tag{7}$$

Furthermore, the weight functions for the attractive and the repulsive components of \mathbf{F}_{ij}^C are defined as $\omega_c(r_{ij}) = 1 - r_{ij}/r_c$ and $\omega_d(r_{ij}) = 1 - r_{ij}/r_d$, respectively. Throughout this work the following cutoff distances are used: $r_{c\rho} = r_d = 0.75$ and $r_c = 1.0$. Particles representing the distinct phases of a multiphase system are assigned a unique numeric ID at initialization to handle the pairwise interactions. For example, in a binary system composed of liquid and solid particles, the force parameters and the cutoff distances are assigned for liquid-liquid, liquid-solid, and solid-solid interactions.

III. PARAMETER MAPPING AND SIMULATION SETUP

A. Parameter mapping

To accurately represent the properties of the fluid, the mDPD parameters have to be chosen carefully by mapping the mDPD parameters to the physical system of interest, i.e., molten CMAS. The physical properties of molten CMAS are taken to be at $1260\,^{\circ}\text{C}$ and the relevant physical properties at this temperature are taken from the experimental work of Naraparaju *et al.* [22]. These are: density $\rho_l = 2690\,\text{kg/m}^3$, surface tension $\sigma_l = 0.46\,\text{N/m}$, and dynamic viscosity $\mu_l = 3.6\,\text{Pa} \cdot \text{s}$. Following Arienti *et al.* [44], reference length [L], mass [M], and time [T] scales are computed to nondimensionalize the system. The reference quantities are defined in terms of the reference units as

$$\rho_{\text{ref}} = \frac{[M]}{[L]^3}; \ \sigma_{\text{ref}} = \frac{[M]}{[T]^2}; \ \nu_{\text{ref}} = \frac{[L]^2}{[T]}. \tag{8}$$

Following this, the nondimensional (mDPD) parameters are defined as

$$\rho = \frac{\rho_l}{\rho_{\text{ref}}} \Rightarrow [M] = [L]^3 \frac{\rho_l}{\rho},\tag{9}$$

$$\sigma = \frac{\sigma_l}{\sigma_{\text{ref}}} \Rightarrow [T]^2 = [M] \frac{\sigma}{\sigma_l},\tag{10}$$

$$\nu = \frac{\nu_l}{\nu_{\text{ref}}} \Rightarrow [T] = [L]^2 \frac{\nu_l}{\nu_l}.$$
 (11)

To match both the viscosity and surface tension we eliminate [T] from Eqs. (10) and (11) and then substitute [M] from Eq. (9). The resulting equation is given by

$$[L] = \left(\frac{\nu_l}{\nu}\right)^2 \frac{\rho_l}{\rho} \frac{\sigma}{\sigma_l}.$$
 (12)

Clearly, from Eq. (12) [L] can be estimated from ρ , σ , and ν which are computed a posteriori from mDPD simulations and are not imposed as done in continuum-based methods.

To compute the kinematic viscosity ν of the mDPD fluid, a doubly periodic Poiseuille (DPP) flow [45] is setup. This has an exact solution given by

$$u(y) = \frac{f_x y d}{2v} \left(1 - \frac{|y|}{d} \right),\tag{13}$$

where f_x is the body force and d is the half-channel height. To simulate this flow, mDPD particles are initialized in a doubly periodic box of size $30 \times 80 \times 10$ mDPD units along the x-, y-, and z-directions as shown in Fig. 2(a). Above the half-channel height, the particles are driven by a body force f_x imposed along the positive x-direction, and below the half-channel height, f_x is imposed along the negative x-direction. The system is allowed to relax for 10 mDPD time units without the action of any body force to dissipate the additional energy from initialization. Following this, the body force is applied and the system is run for 40 mDPD time units before it reaches a steady state. Upon reaching the steady state, the average velocity along the y-direction is computed by binning the particles into 80 slabs in the xz-direction for another 40 mDPD time units. Finally, the kinematic viscosity v is computed from the least-squares approximation to the mDPD solution and is shown in Fig. 2(b). For a simulation that is carried out with A = -40, B = 25, $\gamma = 20$, $k_BT = 1$, $r_c = 1.0$, $r_d = r_{c\rho} = 0.75$, $r_D = 1.45$, and $\rho = 6.74$, the resulting viscosity is v = 29.093 in mDPD units. The kinematic viscosity computed for different cutoff distances r_D is shown in Fig. 2(c).

The surface tension, on the other hand, is computed using the thin liquid film method [46], wherein the surface tension is computed from the normal and tangential stresses across the plane using the Irving-Kirkwood equation given by

$$\sigma = \int_{0}^{L_{z}} [p_{zz} - 0.5(p_{xx} + p_{yy})]dz, \tag{14}$$

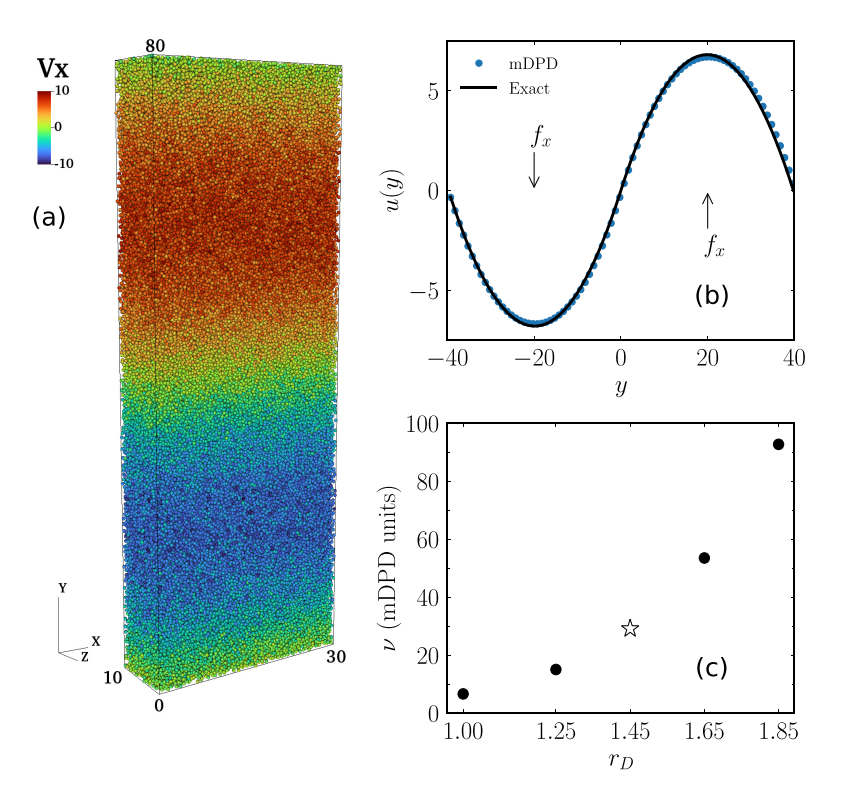


FIG. 2. (a) Setup of the DPP flow. The particles are colored by their velocities along the *x*-direction. (b) The mDPD and the exact solution of the flow at steady state. (c) Viscosity ν computed from the curve-fit to the mDPD solution for different cutoff distances r_D . The open star corresponds to $r_D = 1.45$ and $\nu = 29.093$ in mDPD units, i.e., the values used for the molten CMAS drops.

where L_z is the length of the domain along the z-direction, p_{zz} is the normal, and p_{xx} , p_{yy} are the tangential stress components. The mDPD particles are initialized in a triply periodic domain of size $52 \times 52 \times 20$ mDPD units as shown in Fig. 3(a). The mDPD simulations are run with same parameters and cutoff distances as in the DPP flow. As done in the case of the DPP flow, the system is relaxed for 10 mDPD time units and the time-averaged surface tension is computed for the next 40 mDPD time units. The distribution of σ for different attraction parameters A is shown in Fig. 3(b) and the corresponding mean values are shown in Fig. 3(c). In this work, A = -40 is selected which gives $\langle \sigma \rangle = 9.287 \pm 0.07$ in mDPD units. Based on the physical properties of the molten CMAS droplet and the computed nondimensional properties of the mDPD fluid, the reference units obtained are: $[L] = 17.017 \,\mu\text{m}$, $[M] = 1.964 \times 10^{-8} \,\text{kg}$, and $[T] = 6.297 \,\mu\text{s}$. The physical and the reference quantities are tabulated in Table I.

B. Simulation setup

To examine the spreading behavior of molten CMAS, sessile drop simulations are performed on a smooth substrate. The droplet and the wall are composed of randomly generated preequilibriated mDPD particles. Simulations are carried out with drops of initial radii R=8, 10, and 12 mDPD units, which corresponds to 0.136 mm, 0.17 mm, and 0.204 mm, respectively, in physical units. In experiments, molten CMAS exhibited extensive wetting on most TBC surfaces. The final contact angles observed in these experiments were well-below 90° with some completely wetting the samples. This is in agreement with the available body of experimental work from different groups

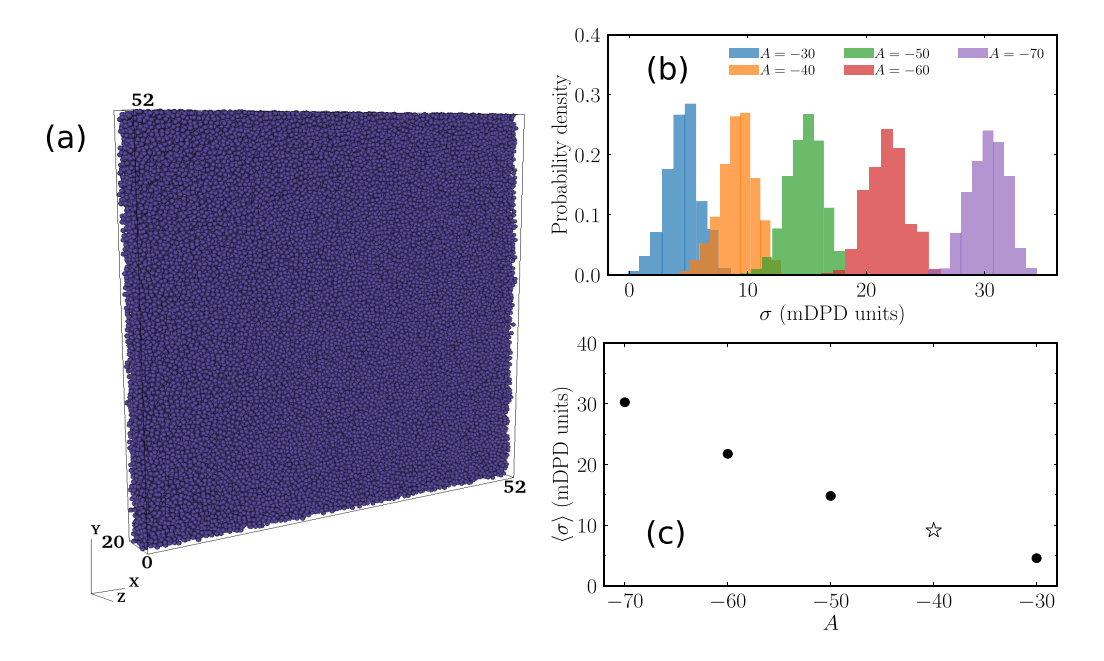


FIG. 3. (a) Setup used in the thin liquid film method. (b) The distribution of σ for different attraction parameter (A) values. (c) Mean values of σ for different A. The open star corresponds to A = -40 and $\langle \sigma \rangle = 9.287$ in mDPD units, i.e., the values value used for the molten CMAS drops.

[21,22,47,48]. In light of this "sandphillic" behavior, three shallow equilibrium contact angles, i.e., $\theta_{\rm eq}=39^{\circ}$, 55°, and 70°, are used to investigate the effect of $\theta_{\rm eq}$ on droplet spreading. To obtain the correct $\theta_{\rm eq}$, the liquid-solid interfacial tension is altered by varying the attraction parameter $A_{\rm ls}$ between the liquid and solid particles. The equilibrium contact angle for different values of $A_{\rm ls}$ is shown in Fig. 4. Collectively, a total of five simulations are performed. All the simulations are carried out with B=25, $\gamma=20$, $k_BT=1$, $r_c=1.0$, $r_d=r_{c\rho}=0.75$, $r_D=1.45$, and $\rho=6.74$. The attraction parameter between the liquid particles $A_{\rm ll}$ is set to the -40 and the same between the liquid and solid particles A_{ls} is set accordingly to obtain the required $\theta_{\rm eq}$. The time integration of the governing equations is carried out using a modified velocity-Verlet algorithm with time step dt = 0.002. For CMAS, the capillary length $l_c=\sqrt{\sigma/(\rho g)}$ is 4.17 mm and hence the effects of gravity on spreading can safely be ignored for the drop sizes under consideration in this work. The Ohnesorge number, defined as Oh = $\mu/\sqrt{\sigma\rho R}$, is a useful indicator to demarcate viscous

TABLE I. Physical and reference properties of molten CMAS.

Property	Physical units	mDPD units
Density ρ	$2690 \mathrm{kg/m^3}$	6.74
Dynamic viscosity μ	3.6 Pa · s	196.08
Kinematic viscosity v	$1.33 \times 10^{-3} \text{ m}^2/\text{s}$	29.093
Surface tension σ	0.46 N/m	9.287
Length [L]	$17.017 \times 10^{-6} \text{ m}$	1.0
Mass [M]	$1.964 \times 10^{-8} \mathrm{kg}$	1.0
Time $[T]$	$6.297 \times 10^{-6} \mathrm{s}$	1.0

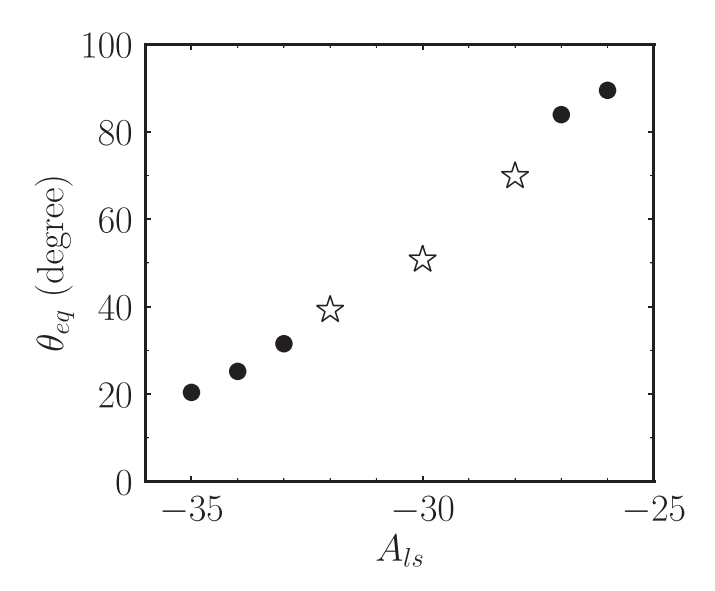


FIG. 4. Equilibrium contact angle is plotted as a function of the mDPD liquid-solid attraction parameter A_{ls} . The open stars correspond to $A_{ls} = -28$, -30, and -32, i.e., the parameters used in the simulations.

and inertial regimes. In this study, Oh = 8.77, 7.85, and 7.16 for R = 0.136 mm, 0.17 mm, and 0.204 mm, respectively.

The mDPD implementation [49] in the massively parallel open source code LAMMPS [50] is used to perform the simulations. Furthermore, the evolution of the contact line and the dynamic contact angle are tracked in this work to investigate the underlying spreading mechanisms. Given the discrete nature of the numerical scheme, approximate curve-fitting approaches are taken to compute the quantities of interest. First to compute the spreading radius r, mDPD particles on the surface of the drop are extracted based on the local number density. The particles with $\rho \in [0.45, 0.6]$ are identified as the surface particles. From these surface particles, a thin layer of particles that are in contact with the solid surface are extracted and fitted to a circle of radius r. To compute the contact angle, first the centroid and the radius of the surface particles are computed by averaging the minimum and maximum spatial positions of the surface particles. Using these values as an initial guess, a sphere is fit to the surface particles. Finally, the contact angle is defined as the angle between the tangent of the fitted sphere and the horizontal wall.

IV. RESULTS

A. Spreading radius

To investigate the spreading behavior of molten CMAS, the spreading radius r is tracked over time. The effect of initial drop size R and the equilibrium contact angle θ_{eq} on the spreading radius r is shown on the log-log plots in Figs. 5(a) and 5(b), respectively. The results in Fig. 5(a) correspond to $\theta_{eq} = 55^{\circ}$ and those in Fig. 5(b) correspond to R = 0.17 mm. As a result of the large viscosity, the spreading occurs over a long time before an equilibrium is reached. The case with $\theta_{eq} = 39^{\circ}$ and R = 0.17 mm takes the longest time owing to the small θ_{eq} . More importantly, two distinct spreading regimes can be identified in these plots. The formation of the neck at the interface during the early moments of CMAS spreading is shown in Fig. 6. At this point, the droplet takes a distinctively nonspherical shape. Once the capillary waves are dissipated, the droplet assumes the shape of a spherical cap.

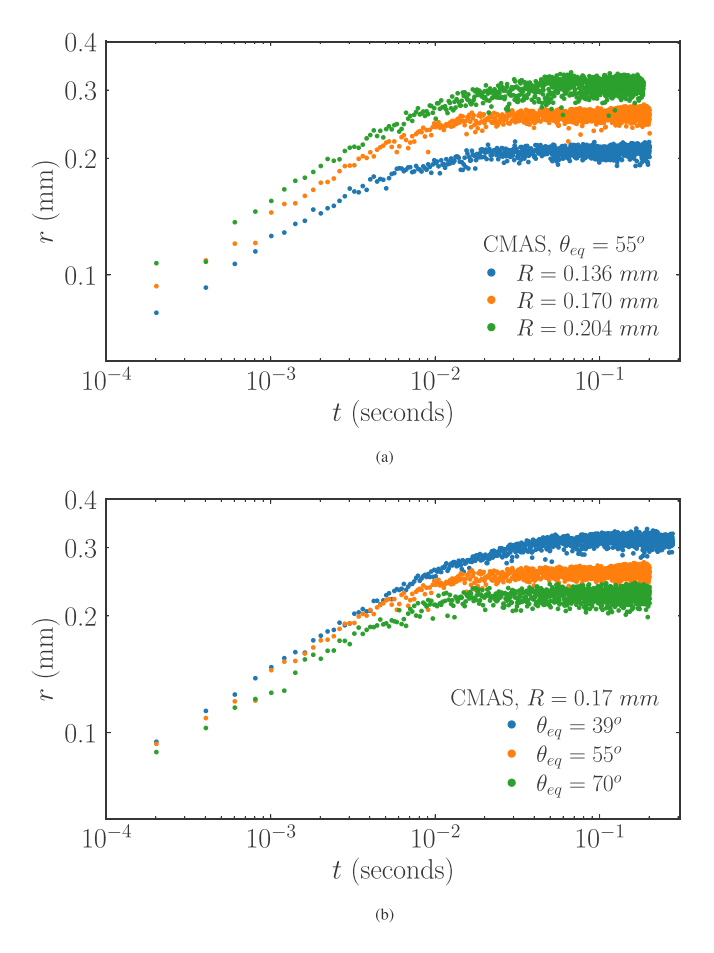


FIG. 5. The effect of (a) initial drop size R and (b) equilibrium contact angle θ_{eq} on the spreading radius is shown on a log-log plot.

To characterize these spreading regimes, well-established scaling laws developed in the context of droplet coalescence are used. In an inertia dominated case, $r/R = f(t/\sqrt{\rho R^3/\sigma}, \theta_{eq})$ whereas in a viscosity dominated case, the temporal evolution is dependent on the viscous timescale $\tau_v = \mu R/\sigma$. Given the large Oh of the CMAS drops in this work, the spreading radius was scaled using the viscous timescale. With this scaling, the spreading radii of different size drops collapse on to a master curve for a given θ_{eq} . This is shown in the log-log plot in Fig. 7(a). This indicates that the contact line motion on a given surface is independent of the drop size. The drops spread over a longer t/τ_v to reach equilibrium due to the effects of large viscosity. By fitting the data to a power law of the form $r/R \sim (t/\tau_v)^{\alpha}$ using least-squares minimization, the exponent α , i.e., the spreading rate is computed both at an early and late time. Figure 7 shows that the slope of the normalized spreading radius changes smoothly from the inertial regime with $\alpha = 0.26$ to the steady state with $\alpha = 0$, which does not change with droplet size R but changes when the equilibrium contact angle θ_{eq} varies. The spreading rate in the inertial regime is in excellent agreement with the experimental results [33] of molten volcanic ash droplets spreading on a smooth Alumina substrate. The experiments report a spreading rate of 0.28 at 1272 °C under viscous scaling. Although the viscosity of volcanic ash greater than that of CMAS (500 Pa·s), the surface tension (0.35–0.37 N/m) and the density (2000–2895 kg/m³) are quite comparable. Compared to the CMAS used in this study, the volcanic ash is characterized by 61% higher SiO₂ and 83% lower CaO by weight percentage which could be

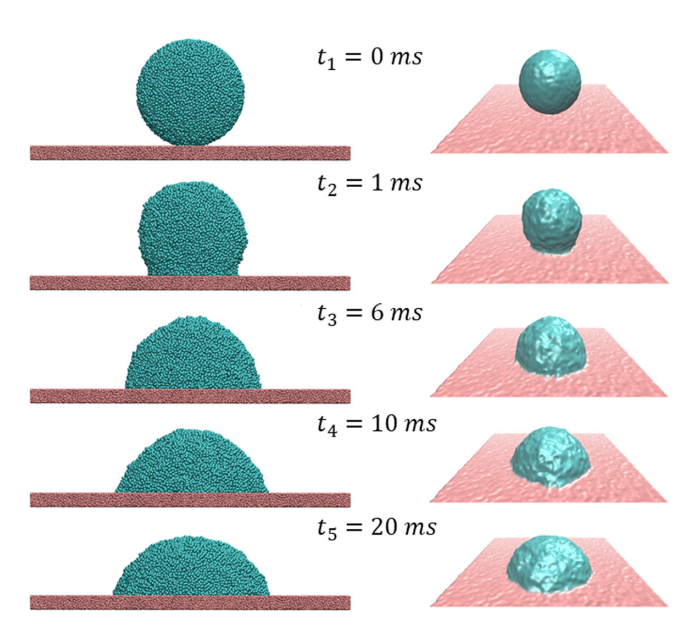


FIG. 6. A cross-section view (left) and an aerial view (right) of the spreading dynamics of a 3D CMAS drop with a radius of R = 0.17 mm on a hydrophilic surface with $\theta_{eq} = 39^{\circ}$.

the reason for higher viscosity of molten volcanic ash. A spreading rate of approximately 0.26 in the inertial regime is followed by a rate of approximately 0.1 in the viscous regime before the drop reaches equilibrium. The spreading rate of $\alpha=0.1$ corresponds to the Tanner's law of spreading for vanishing contact angles wherein the spreading dynamics are controlled by the contact line dissipation. However, no such collapse of data is observed for the spreading radius at different $\theta_{\rm eq}$ as shown in Fig. 7(b). However, the spreading rate in the inertial regime is fairly robust with the curves only diverging once the effects of partial wetting kick-in. Interestingly, Bird *et al.* [7] reported a spreading rate varying between 0.5 and 0.25 for $\theta_{\rm eq}=3^{\circ}-117^{\circ}$. The lower spreading rates were attributed by the authors to the effects of finite equilibrium contact angle. The effects of viscosity on the spreading are discussed in more detail in the next section.

B. Effect of viscosity

In their experiments with viscous fluids ($\mu = 0.3-10.3$ mPa·s), Bird et al. [7] observed inertia dominated spreading. This is evident from the divergence of spreading radius when viscous timescale τ_v is used. Aarts et al. [6], however, observed viscosity dominated coalescence experiments with silicone oil drops with a wide range of viscosities but relatively low surface tension (0.02 N/m). A linear relation between r/R and t/τ_v was observed but the logarithmic dependence, predicted by the theory [12], was not observed. Eddi et al. [8] investigated the spreading of viscous drops (10–1.12 Pa · s) and reported a continuously decreasing exponent ranging between 0.8 and 0.5 in the inertial regime before transitioning sharply to the viscous regime with an exponent consistent with Tanner's law. Following Eddi et al. [8], the spreading rate $\alpha = d \ln r/d \ln t$ is computed. This is shown in Fig. 8(a) as a function time. The spreading rate varies between 0.3 and 0.2 in the inertial regime before plateauing. Due to the high viscosity of CMAS, the transition between the two regimes is smooth and in accordance with experimental evidence. For comparison, experimental data of pure glycerin drop from Eddi et al. [8] is also plotted. The density, dynamic viscosity, and surface tension of the glycerin drop used in the experiments are 1262 kg/m³, 1.12 Pa · s and 0.063 N/m, respectively. This particular data from the experiments was chosen since the viscosities of glycerin and CMAS are of the same order-of-magnitude although the surface tension of CMAS

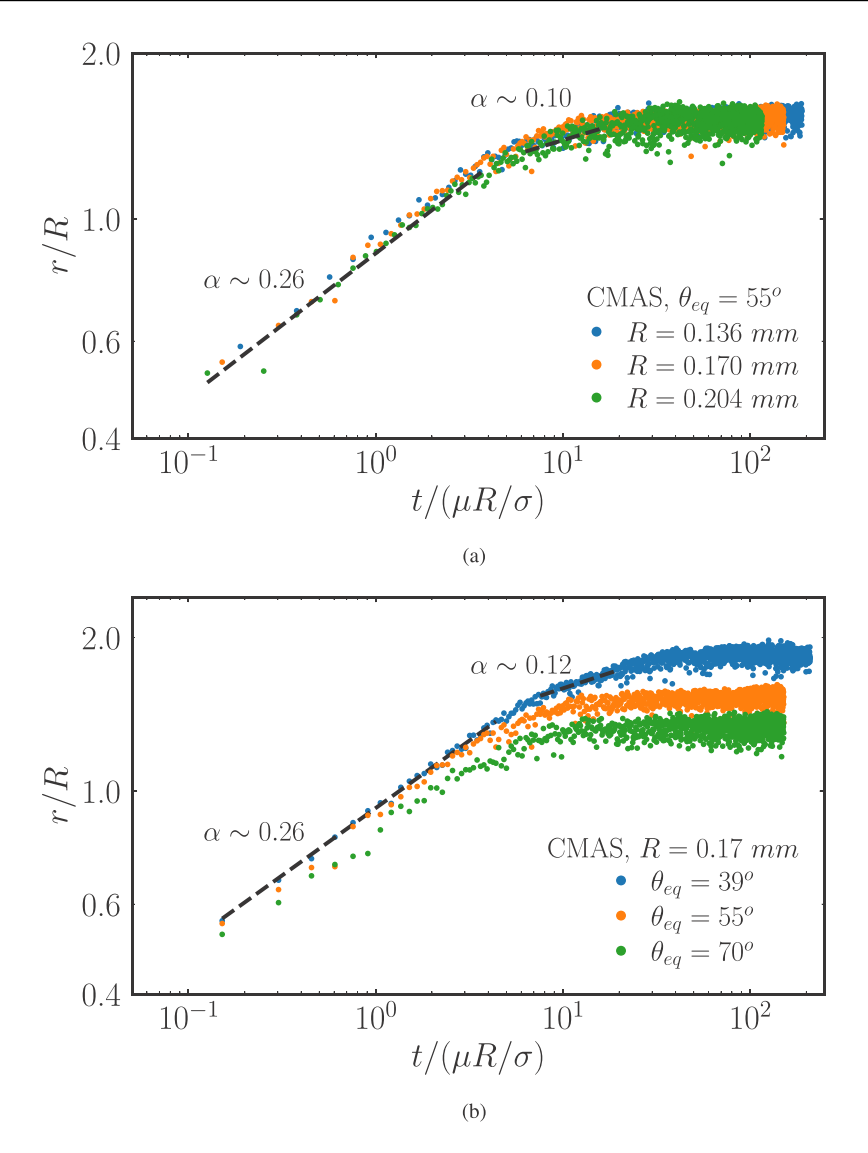


FIG. 7. Nondimensional spreading radius as a function of time rescaled using the viscous timescale is shown on a log-log plot for (a) R=0.136 mm, 0.17 mm and 0.204 mm at $\theta_{\rm eq}=55^{\circ}$ and (b) $\theta_{\rm eq}=36^{\circ}$, 55° , and 70° at R=0.17 mm. The least-squares fit to the power law in the inertial and viscous regimes are shown in dashed black lines along with the exponent α of the power law.

is still seven times larger. Clearly, the CMAS drops exhibit a lower rate of spreading compared to the glycerin drop. Since the simulations are of partially wetting fluids, the CMAS drops reach equilibrium, i.e., $\alpha = 0$, unlike the glycerin drop from experiments which is in a complete wetting configuration and takes longer to reach equilibrium.

When, the spreading rate α is plotted as a function of nondimensional spreading radius r/R the data collapses for different initial radii again in line with the experimental data. This is shown in Fig. 8(b). The solid line in the plot is referred to as the "effective exponent" and is defined as

$$\alpha = \frac{\ln \frac{r}{R}}{\ln \frac{r}{R} - 1}.\tag{15}$$

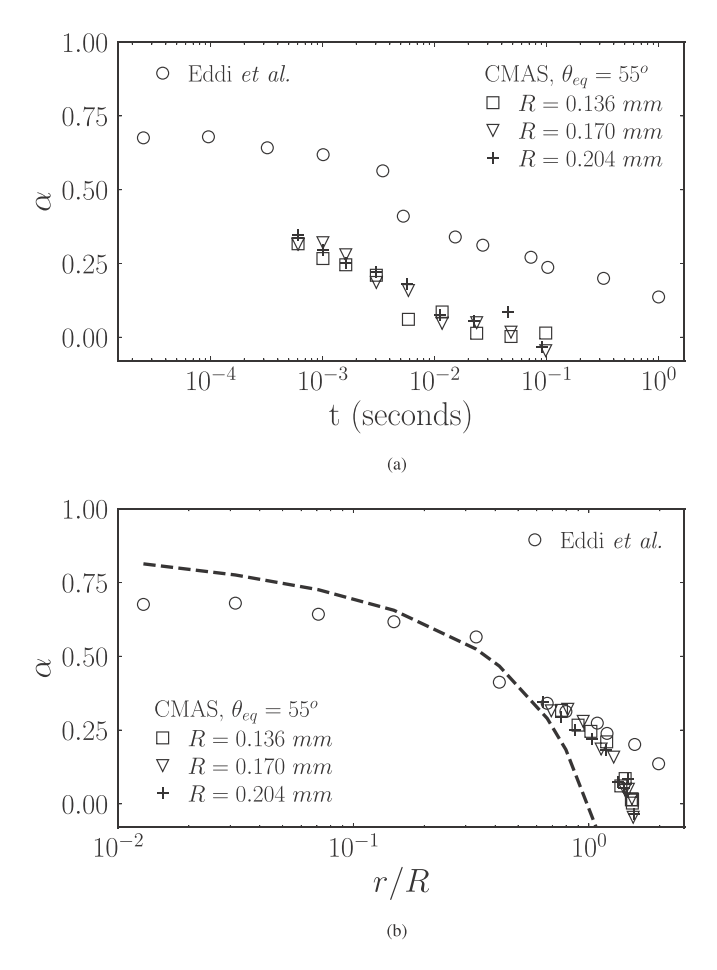


FIG. 8. Spreading rate as a function of (a) time and (b) nondimensional spreading radius r/R is shown on a semilogarithmic plot. The dashed line in panel (b) corresponds to Eq. (15). The spreading data of pure glycerin drop (R=0.5 mm, $\mu=1.12$ Pa·s, $\sigma=0.063$ N/m, and $\rho=1262$ kg/m³) from Eddi *et al.* [8] is represented by the open circles.

This equation is obtained by applying the definition of the spreading rate $\alpha = d \ln r/d \ln t$ to Eq. (15). The experimental data from Eddi *et al.* [8] at lower viscosities agrees well with the curve in the inertial regime indicating the effects of logarithmic correction. However, significant deviations from curve appear at higher viscosities. The effects of logarithmic correction on the spreading radius are not observed in this work since the correction is relevant in the asymptotic limit. Aarts *et al.* [6] estimate these effects to be prominent at $r \leq 0.03R$ which is about 6 μ m for the largest drop size used in the simulations. Unfortunately, this level of spatial resolution was not realized in the simulations.

C. Contact angle evolution

The evolution of the contact angle is shown in Fig. 9. At early time, the contact angle evolution is identical for all the curves with the differences appearing later on due to the effects of partial wetting again reinforcing the observation that the early-time dynamics are independent of the equilibrium contact angle. To investigate the dynamics of the moving contact line the contact line velocity u_{cl} is

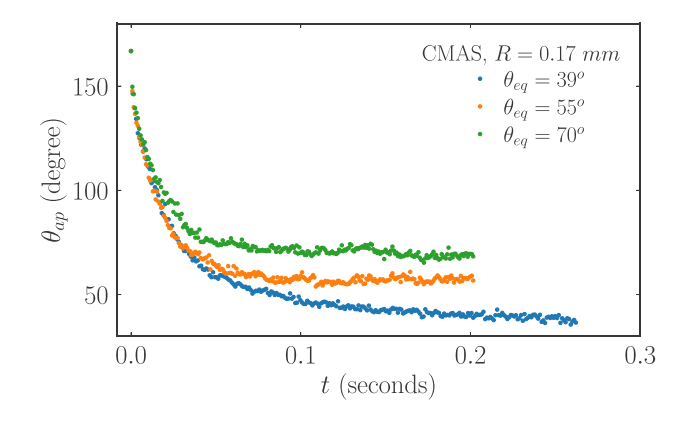


FIG. 9. Time evolution of the apparent contact angle θ_{ap} .

computed by taking a time-derivative of the spreading radius. The relationship between u_{cl} and θ_{ap} is shown in Fig. 10(a) and as expected the contact line motion seizes as $\theta_{ap} \to \theta_{eq}$.

When the viscosity of the surrounding fluid is negligible compared to that of the drop, Cox [13] derived an expression for contact angle evolution which is given by

$$g(\theta) = g(\theta_m) + \operatorname{Ca} \ln(x/L),$$
 (16)

where θ_m is the microscopic contact angle and x, L correspond to macroscopic and microscopic length scales. The function $g(\theta)$ is defined as

$$g(\theta) = \int_0^\theta \frac{x - \sin x \cos x}{2 \sin x} dx. \tag{17}$$

For $\theta < 135^\circ$, $g(\theta)$ can be approximated as $\theta^3/9$ within 1% error. A simpler representation of the Cox's relation was presented by Hoffman [51] and Kistler [52]. Hoffman observed that the contact angle data from his experiments closely followed a general curve when plotted as a function of Ca with a certain shift factor. An empirical fit to this curve was obtained by Kistler and is given by

$$\theta_{\rm ap} = f_H \left[\text{Ca} + f_H^{-1}(\theta_{\rm eq}) \right], \tag{18}$$

where f_H is referred to as the Hoffman function defined as

$$f_H(x) = \arccos\left\{1 - 2\tanh\left[5.16\left(\frac{x}{1 + 1.31x^{0.99}}\right)^{0.706}\right]\right\}.$$
 (19)

In this work, the inverse Hoffman function f_H^{-1} is approximated using the Hoffman-Voinov-Tanner law [53] which is valid for Ca < 1 and is given by

$$f_H^{-1} = \frac{\theta_{\text{eq}}^3}{c_T},$$
 (20)

where c_T is a constant assumed to be about 72 rad³. In Cox's theory, there are no restrictions placed on the microscopic contact angle: it can be constant or velocity-dependent. In Eq. (18), which has an identical functional form as Eq. (16), θ_{eq} is used instead of θ_m . Following this, the contact angle is plotted as a function of Ca shifted by the approximate inverse Hoffman function given by Eq. (20) and is shown in Fig. 10(b). The Hoffman function, given by Eq. (19) is overlaid on the simulation data and is represented by the solid black curve. A very good agreement is observed between the simulation results and the model. This indicates that the Cox's theory is still valid for molten CMAS.

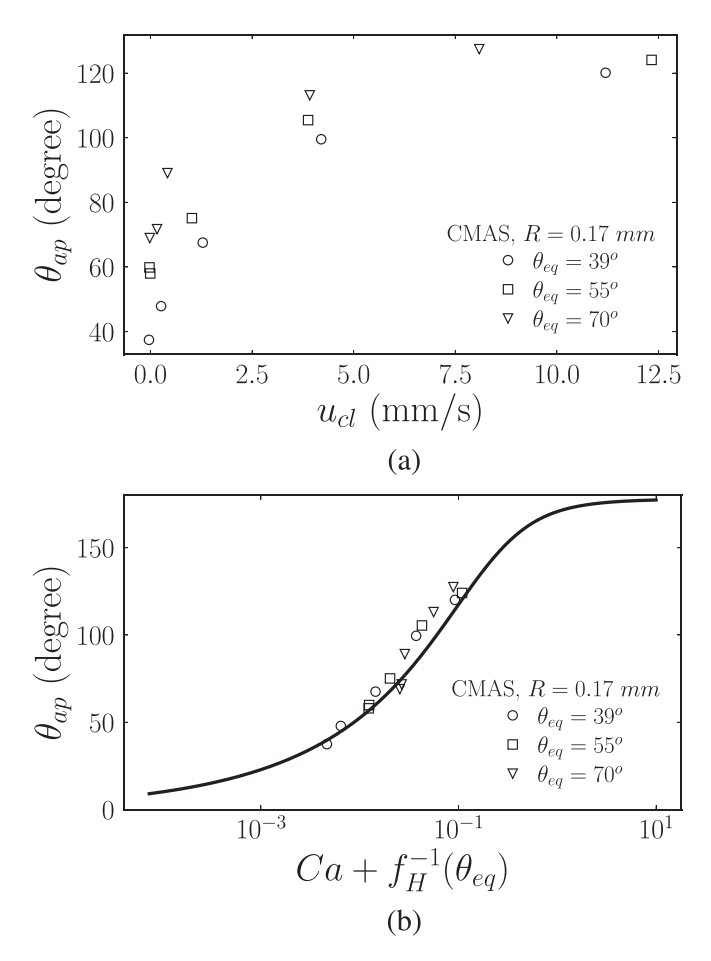


FIG. 10. (a) The apparent contact angle θ_{ap} is plotted as a function of the contact line velocity u_{cl} for drops with different equilibrium contact angles θ_{eq} . (b) The apparent contact angle θ_{ap} is plotted as a function of the capillary number Ca. The solid black curve is the model proposed by Kistler and is given by Eqs. (18)–(20).

V. CONCLUDING REMARKS

A detailed numerical study was conducted to investigate the spreading dynamics of molten CMAS on smooth surfaces using many-body dissipative dynamics. To this end, sessile drop simulations were performed at isothermal conditions with different drop sizes and equilibrium contact angles to investigate the effects of initial drop size and partial wetting. In particular, the temporal evolution of the spreading radius and the dynamic contact angle were studied and compared with the existing theory and experiments. Modeling CMAS, which has very high surface tension in addition to being highly viscous and dense, required an equally large viscosity in the simulations typically unseen in mDPD community.

The spreading of molten CMAS is clearly characterized by two distinct, inertia-dominated and viscosity-dominated, regimes. In agreement with experimental evidence, the contact line spreading was observed to be independent of the drop size throughout the entire spreading phase. This is evident from the data collapse in Fig. 7(a), wherein a characteristic viscous timescale τ_v was used to rescale the data. This indicates a quantitative agreement with the theory of viscous coalescence of drops. Although the spreading radius does not exhibit such collapse for different equilibrium contact angles, the spreading in the inertial regime is quite identical with all the curves exhibiting an overall

slope of 0.26. The spreading rate in the inertial regime agrees well with the available experimental data of molten volcanic ash spreading on smooth surfaces which is between 0.26 and 0.31. The curves in Fig. 7(b) begin to diverge as the effects of partial wettability become dominant. Within the inertial regime, a nonunique spreading rate α was observed which is consistent with experiments. The value of α in this work is between 0.3 and 0.2 in the inertial regime which is lower than what was observed in the experiments of Eddi *et al.* [8]. This is attributed to the higher viscosity and surface tension of CMAS. The logarithmic corrections on the spreading were not observed when α is plotted as a function of r/R due to the lack of sufficient resolution to capture the very early-time evolution of the contact line. Despite the unique properties of CMAS, a good agreement between the simulation results and theory was observed for the dynamic contact angle evolution. The simulation results are in good agreement with Hoffman's model for dynamic contact angle.

The evidence presented in this work indicates that the spreading of molten CMAS is in good agreement with that of other relatively lower viscosity fluids. This study further reinforces the analogous behavior between droplet coalescence and droplet spreading. To gain a more fundamental insight in to the role of interfacial dynamics on CMAS attack, the effects of surface roughness, pressure, heat transfer, and phase change on the moving contact line need to be investigated and will be the focus of future research.

ACKNOWLEDGMENTS

Authors A.F. and R.B.K. acknowledge the support received from the U.S. Army Research Office Mathematical Sciences Division for this research through grant number W911NF1910225. L.B., A.G., and M.M. were supported by the U.S. Army Research Laboratory 6.1 basic research program in propulsion sciences. Z.L. acknowledges the support from the NSF Grant No. OAC-2103967 and the NASA Project No. 80NSSC21M0153. The authors gratefully acknowledge the resources and support provided by Department of Defense Supercomputing Resource Center (DSRC) through use of "Narwhal" as part of the 2022 Frontier Project, Large-scale Integrated Simulations of Transient Aerothermodynamics in Gas Turbine Engines. The authors acknowledge the support received from DoD's Strategic Environmental Research and Development Program (SERDP) for this research. The authors thank Dr. Andrew Wright for providing the experimental data and images from the high-temperature contact angle measurement experiments of CMAS. The views and conclusions contained in this document are those of the authors and should not be interpreted as representing the official policies or positions, either expressed or implied, of the U.S. Army Research Laboratory or the U.S. Government. The U.S. Government is authorized to reproduce and distribute reprints for Government purposes notwithstanding any copyright notation herein.

^[1] S. Nishimoto and B. Bhushan, Bioinspired self-cleaning surfaces with superhydrophobicity, superoleophobicity, and superhydrophilicity, RSC Adv. 3, 671 (2013).

^[2] R. C. Chiechi, E. A. Weiss, M. D. Dickey, and G. M. Whitesides, Eutectic gallium-indium (EGaIn): A moldable liquid metal for electrical characterization of self-assembled monolayers, Angew. Chem., Int. Ed. 47, 142 (2008).

^[3] E. K. Sackmann, A. L. Fulton, and D. J. Beebe, The present and future role of microfluidics in biomedical research, Nature (London) 507, 181 (2014).

^[4] D. Lohse, Fundamental fluid dynamics challenges in inkjet printing, Annu. Rev. Fluid Mech. 54, 349 (2022).

^[5] A.-L. Biance, C. Clanet, and D. Quéré, First steps in the spreading of a liquid droplet, Phys. Rev. E 69, 016301 (2004).

^[6] D. G. A. L. Aarts, H. N. W. Lekkerkerker, H. Guo, G. H. Wegdam, and D. Bonn, Hydrodynamics of Droplet Coalescence, Phys. Rev. Lett. 95, 164503 (2005).

- [7] J. C. Bird, S. Mandre, and H. A. Stone, Short-Time Dynamics of Partial Wetting, Phys. Rev. Lett. 100, 234501 (2008).
- [8] A. Eddi, K. G. Winkels, and J. H. Snoeijer, Short time dynamics of viscous drop spreading, Phys. Fluids 25, 013102 (2013).
- [9] H. Ding and P. D. Spelt, Inertial effects in droplet spreading: A comparison between diffuse-interface and level-set simulations, J. Fluid Mech. **576**, 287 (2007).
- [10] J. De Coninck and T. D. Blake, Wetting and molecular dynamics simulations of simple liquids, Annu. Rev. Mater. Res. 38, 1 (2008).
- [11] K. G. Winkels, J. H. Weijs, A. Eddi, and J. H. Snoeijer, Initial spreading of low-viscosity drops on partially wetting surfaces, Phys. Rev. E **85**, 055301(R) (2012).
- [12] J. Eggers, J. R. Lister, and H. A. Stone, Coalescence of liquid drops, J. Fluid Mech. 401, 293 (1999).
- [13] R. Cox, The dynamics of the spreading of liquids on a solid surface. Part 1. Viscous flow, J. Fluid Mech. **168**, 169 (1986).
- [14] D. Bonn, J. Eggers, J. Indekeu, J. Meunier, and E. Rolley, Wetting and spreading, Rev. Mod. Phys. 81, 739 (2009).
- [15] Y. D. Shikhmurzaev, Moving contact lines and dynamic contact angles: A "litmus test" for mathematical models, accomplishments, and new challenges, Eur. Phys. J.: Spec. Top. 229, 1945 (2020).
- [16] Y. Si, C. Yu, Z. Dong, and L. Jiang, Wetting and spreading: Fundamental theories to cutting-edge applications, Curr. Opin. Colloid Interface Sci. 36, 10 (2018).
- [17] A. Vyas, V. Garg, S. B. Ghosh, and S. Bandyopadhyay-Ghosh, Photopolymerizable resin-based 3D printed biomedical composites: Factors affecting resin viscosity, Mater. Today: Proc. 62, 1435 (2022).
- [18] N. Jain, A. Le Moine, G. Chaussonnet, A. Flatau, L. Bravo, A. Ghoshal, M. Walock, M. Murugan, and P. Khare, A critical review of physical models in high temperature multiphase fluid dynamics: Turbulent transport and particle-wall interactions, Appl. Mech. Rev. 73, 040801 (2021).
- [19] A. Nieto, R. Agrawal, L. Bravo, C. Hofmeister-Mock, M. Pepi, and A. Ghoshal, Calcia-magnesiaalumina-silicate (CMAS) attack mechanisms and roadmap toward sandphobic thermal and environmental barrier coatings, Int. Mater. Rev. 66, 451 (2021).
- [20] N. P. Padture, M. Gell, and E. H. Jordan, Thermal barrier coatings for gas-turbine engine applications, Science 296, 280 (2002).
- [21] Y. Kang, Y. Bai, G. Du, F. Yu, C. Bao, Y. Wang, and F. Ding, High temperature wettability between CMAS and YSZ coating with tailored surface microstructures, Mater. Lett. 229, 40 (2018).
- [22] R. Naraparaju, J. J. G. Chavez, P. Niemeyer, K.-U. Hess, W. Song, D. B. Dingwell, S. Lokachari, C. Ramana, and U. Schulz, Estimation of CMAS infiltration depth in EB-PVD TBCs: A new constraint model supported with experimental approach, J. Eur. Ceram. Soc. 39, 2936 (2019).
- [23] A. Ghoshal, M. Murugan, M. J. Walock, A. Nieto, B. D. Barnett, M. S. Pepi, J. J. Swab, D. Zhu, K. A. Kerner, C. R. Rowe *et al.*, Molten particulate impact on tailored thermal barrier coatings for gas turbine engine, J. Eng. Gas Turbines Power **140**, 022601 (2018).
- [24] M. Murugan, A. Ghoshal, M. Walock, L. G. Bravo, R. Koneru, N. Jain, C. Mock, M. Pepi, A. Nieto, A. Flatau *et al.*, In search of durable sandphobic thermal/environmental barrier coatings for rotorcraft gas turbine engines, in *Proceedings of the AIAA Scitech Forum* (2021), p. 0874.
- [25] P. B. Warren, Vapor-liquid coexistence in many-body dissipative particle dynamics, Phys. Rev. E 68, 066702 (2003).
- [26] C. Lin, K. Zhang, X. Chen, L. Xiao, S. Chen, J. Zhu, and T. Zou, Reducing droplet contact time and area by craterlike surface structure, Phys. Rev. Fluids 6, 083602 (2021).
- [27] K. Zhang, Z. Li, M. Maxey, S. Chen, and G. E. Karniadakis, Self-cleaning of hydrophobic rough surfaces by coalescence-induced wetting transition, Langmuir 35, 2431 (2019).
- [28] C. Lin, D. Cao, D. Zhao, P. Wei, S. Chen, and Y. Liu, Dynamics of droplet impact on a ring surface, Phys. Fluids 34, 012004 (2022).
- [29] G. Yi, Z. Cai, Z. Gao, Z. Jiang, X. Huang, and J. J. Derksen, Droplet impingement and wetting behavior on a chemically heterogeneous surface in the Beyond–Cassie–Baxter regime, AIChE J. 66, e16263 (2020).
- [30] T. W. Munuhe, R.-H. Chen, L. Zhu, and R. Ma, Modeling molten droplet spreading and infiltration into nonisothermal thermal barrier coatings, Int. J. Heat Mass Transf. 182, 121942 (2022).

- [31] M. R. Kabir, A. K. Sirigiri, R. Naraparaju, and U. Schulz, Flow kinetics of molten silicates through thermal barrier coating: A numerical study, Coatings 9, 332 (2019).
- [32] G. Chaussonnet, L. Bravo, A. Flatau, R. Koch, and H.-J. Bauer, Smoothed particle hydrodynamics simulation of high velocity impact dynamics of molten sand particles, Energies 13, 5134 (2020).
- [33] W. Song, Y. Lavallee, F. B. Wadsworth, K.-U. Hess, and D. B. Dingwell, Wetting and spreading of molten volcanic ash in jet engines, J. Phys. Chem. Lett. **8**, 1878 (2017).
- [34] P. Hoogerbrugge and J. Koelman, Simulating microscopic hydrodynamic phenomena with dissipative particle dynamics, Europhys. Lett. 19, 155 (1992).
- [35] J. Zhao, S. Chen, K. Zhang, and Y. Liu, A review of many-body dissipative particle dynamics (MDPD): Theoretical models and its applications, Phys. Fluids 33, 112002 (2021).
- [36] Z. Li, X. Bian, B. Caswell, and G. E. Karniadakis, Construction of dissipative particle dynamics models for complex fluids via the Mori–Zwanzig formulation, Soft Matter 10, 8659 (2014).
- [37] P. Español and M. Revenga, Smoothed dissipative particle dynamics, Phys. Rev. E 67, 026705 (2003).
- [38] P. Español and P. B. Warren, Perspective: Dissipative particle dynamics, J. Chem. Phys. 146, 150901 (2017).
- [39] Y. Sui, H. Ding, and P. D. Spelt, Numerical simulations of flows with moving contact lines, Annu. Rev. Fluid Mech. 46, 97 (2014).
- [40] Z. Li, X. Bian, Y.-H. Tang, and G. E. Karniadakis, A dissipative particle dynamics method for arbitrarily complex geometries, J. Comput. Phys. 355, 534 (2018).
- [41] R. D. Groot and P. B. Warren, Dissipative particle dynamics: Bridging the gap between atomistic and mesoscopic simulation, J. Chem. Phys. 107, 4423 (1997).
- [42] P. Español and P. Warren, Statistical mechanics of dissipative particle dynamics, Europhys. Lett. 30, 191 (1995).
- [43] L. B. Lucy, A numerical approach to the testing of the fission hypothesis, Astron. J. 82, 1013 (1977).
- [44] M. Arienti, W. Pan, X. Li, and G. Karniadakis, Many-body dissipative particle dynamics simulation of liquid/vapor and liquid/solid interactions, J. Chem. Phys. **134**, 204114 (2011).
- [45] Z. Li, Y.-H. Tang, H. Lei, B. Caswell, and G. E. Karniadakis, Energy-conserving dissipative particle dynamics with temperature-dependent properties, J. Comput. Phys. 265, 113 (2014).
- [46] A. Ghoufi and P. Malfreyt, Calculation of the surface tension from multibody dissipative particle dynamics and Monte Carlo methods, Phys. Rev. E **82**, 016706 (2010).
- [47] B. Zhang, W. Song, and H. Guo, Wetting, infiltration and interaction behavior of CMAS toward columnar YSZ coatings deposited by plasma spray physical vapor, J. Eur. Ceram. Soc. 38, 3564 (2018).
- [48] B. Yin, M. Sun, W. Zhu, L. Yang, and Y. Zhou, Wetting and spreading behaviour of molten CMAS toward thermal barrier coatings and its influencing factors, Results Phys. 26, 104365 (2021).
- [49] Z. Li, G.-H. Hu, Z.-L. Wang, Y.-B. Ma, and Z.-W. Zhou, Three dimensional flow structures in a moving droplet on substrate: A dissipative particle dynamics study, Phys. Fluids **25**, 072103 (2013).
- [50] A. P. Thompson, H. M. Aktulga, R. Berger, D. S. Bolintineanu, W. M. Brown, P. S. Crozier, P. J. in't Veld, A. Kohlmeyer, S. G. Moore, T. D. Nguyen *et al.*, LAMMPS—A flexible simulation tool for particle-based materials modeling at the atomic, meso, and continuum scales, Comput. Phys. Commun. 271, 108171 (2022).
- [51] R. L. Hoffman, A study of the advancing interface. I. Interface shape in liquid–gas systems, J. Colloid Interface Sci. **50**, 228 (1975).
- [52] S. F. Kistler, Hydrodynamics of wetting, in *Wettability*, edited by J. C. Berg (Marcel Dekker, New York, 1993), pp. 311–429.
- [53] J. Göhl, A. Mark, S. Sasic, and F. Edelvik, An immersed boundary based dynamic contact angle framework for handling complex surfaces of mixed wettabilities, Int. J. Multiphase Flow 109, 164 (2018).